THE UNIVERSITY of TENNESSEE at CHATTANOOGA
COLLEGE of ENGINEERING and COMPUTER SCIENCE

SIMCENTER
NATIONAL CENTER for COMPUTATIONAL ENGINEERING

Adjoint Based Shape Optimization for Electromagnetic Problems using High-order Discontinuous Galerkin Methods

A Technical Report by

Li Wang
and
W. Kyle Anderson

UTC-CECS-SimCenter-2009-03
July 2009

GRADUATE SCHOOL OF COMPUTATIONAL ENGINEERING
701 East M.L. King Boulevard • Chattanooga, TN 37403

Adjoint Based Shape Optimization for Electromagnetic Problems using High-order Discontinuous Galerkin Methods

Li Wang * *and* W. Kyle Anderson†
SimCenter: National Center for Computational Engineering
University of Tennessee at Chattanooga, Chattanooga, TN, 37403

Nomenclature

b	=	Hicks-Henne bump function	$\mathbf{R}$	=	discretized spatial residual
B_0	=	amplitude of a magnetic wave	$\mathbf{R}_e$	=	discretized unsteady residual
c	=	speed of light	$\mathbf{q}$	=	conservative electromagnetic variables
$\mathbf{D}$	=	design variables	T	=	time period
D_0	=	amplitude of an electric wave	α, β, ω	=	parameters for electric and magnetic waves
K	=	mesh stiffness matrix	Δt	=	time-step size
L	=	objective functional	$\lambda_{\mathbf{q}}$, λ_x	=	primal-adjoint and mesh-adjoint variables
m, n	=	integers related to wave numbers	ϕ	=	basis function
M	=	mass matrix	ε, μ	=	permittivity and permeability
N	=	number of time steps	$*$	=	target values
N_s	=	number of surface grid points	$\tilde{}$	=	modal coefficients
$\mathbf{x}$	=	Cartesian coordinates = (x, y)	s, q	=	surface grid points and additional quadrature points

Introduction

In recent years, discontinuous Galerkin (DG) methods have received considerable interests in solving a wide range of convection-dominated problems, such as in computational fluid dynamics [1–3] and electromagnetics [4]. The main benefits of using the DG methods arises from their capability of obtaining optimal error convergence rates and suitability for efficient parallel computing. In addition, sensitivity analysis techniques enable better understanding of the impacts of shape or material parameters to the results of the numerical simulations, thus becoming a potentially indispensable component for the overall design process. The recent work [5] developed a discrete adjoint approach for high-order discontinuous Galerkin discretizations associated with the use of unstructured curvilinear meshes, and the developed techniques were applied to unsteady inviscid flow design problems.

The purpose of the work presented in this report is to extend the research described in references [5] and [6] for applications to Maxwell's equations. The accuracy of the DG scheme is examined to demonstrate that the design order is achieved through 5^{th} order accuracy. A time-dependent adjoint method is also developed to obtain sensitivity derivatives, which are subsequently coupled with a formal optimization procedure to determine the shape of an airfoil by matching a desired magnetic field on the airfoil surface over a specified time period.

Equations and Discretizations

The following conservative form of the two-dimensional source-free Maxwell equations for a transverse electric (TE) field is considered:

$$\frac{\partial \mathbf{q}(\mathbf{x},t)}{\partial t} + \frac{\partial \mathbf{F}(\mathbf{q}(\mathbf{x},t))}{\partial x} + \frac{\partial \mathbf{G}(\mathbf{q}(\mathbf{x},t))}{\partial y} = 0 \tag{1}$$

where $\mathbf{q}$ is the vector of the electric flux density and magnetic induction:

$$\mathbf{q} = \{D_x, D_y, B_z\}^T \tag{2}$$

and the Cartesian flux vector $\vec{\mathbf{F}} = (\mathbf{F}, \mathbf{G})$ is given by,

*Research Assistant Professor, University of Tennessee at Chattanooga, AIAA Member, email: Li-Wang@utc.edu
†Professor, University of Tennessee at Chattanooga, AIAA Associate Fellow, email: Kyle-Anderson@utc.edu

$$\mathbf{F} = \{0, B_z/\mu, D_y/\varepsilon\}^T \quad \text{and} \quad \mathbf{G} = \{-B_z/\mu, 0, -D_x/\varepsilon\}^T \tag{3}$$

where ε and μ denote the permittivity and permeability, respectively, which are set to be constant (and equal to one) due to homogeneous materials being considered in the current work. The electric and magnetic field constants satisfy the relation $\varepsilon_0 \mu_0 c^2 = 1$ in vacuum, where c denotes the speed of light.

In the discontinuous Galerkin method, the solution approximation, $\mathbf{q}_p$, is expanded as a series of modal solution coefficients and hierarchical basis functions $\{\phi_i\}$ [7], expressed as,

$$\mathbf{q}_p = \sum_{i=1}^{M} \tilde{\mathbf{q}}_{p_i} \phi_i(\mathbf{x}) \tag{4}$$

then a discontinuous Galerkin weak formulation to this problem is written as,

$$\int_{\Omega_k} \phi_j \frac{\partial \mathbf{q}_p}{\partial t} d\Omega_k - \int_{\Omega_k} \left[\frac{\partial \phi_j}{\partial x} \mathbf{F}(\mathbf{q}_p) + \frac{\partial \phi_j}{\partial y} \mathbf{G}(\mathbf{q}_p) \right] d\Omega_k + \int_{\partial\Omega_k} \phi_j \mathbf{H}(\mathbf{q}_p^+, \mathbf{q}_p^-, \mathbf{n}) dS = 0 \tag{5}$$

for each element (e.g. k) in the computational domain. The discontinuities at elemental boundaries, as denoted by the interior and exterior traces $\mathbf{q}_p^+$ and $\mathbf{q}_p^-$, are resolved by the implementation of a Riemann flux function such as Lax-Friedrichs [8] or Roe [9]. For edges or faces coinciding with physical boundaries, a perfectly conducting wall condition is applied, where the tangential components of the electric field vanish, expressed as:

$$(D_x/\varepsilon, D_y/\varepsilon)^T \times (n_x, n_y)^T = 0 \qquad \text{or} \qquad n_x D_y/\varepsilon - n_y D_x/\varepsilon = 0 \tag{6}$$

where $\mathbf{n} = (n_x, n_y)^T$ represents the unit normal vector outward to the boundary. The evaluation of the first derivatives, volume and face integrals in Eq. (5) requires a reference-to-physical transformation for each individual element in the computational domain, given by,

$$\mathbf{x}_k = \sum_{i=1}^{M} \tilde{\mathbf{x}}_{k_i} \phi_i \tag{7}$$

and additional surface quadrature points are used for determining the geometric transformation of high-order curved boundary elements [5]. As a consequence, the variation of additional surface quadrature points and the effects to the objective sensitivities must be considered when the surface geometry is deformed.

Equation (5) can be written in the following ordinary differential equation (ODE) form as:

$$M \frac{d\tilde{\mathbf{q}}_p}{dt} + \mathbf{R}(\tilde{\mathbf{q}}_p) = 0 \tag{8}$$

where $\mathbf{R}$ represents the discretized spatial residual and M denotes the mass matrix. The time integration is performed using an implicit, second-order backwards difference Euler (BDF2) scheme. The formulation for the BDF2 scheme is derived by starting from the set of ODEs given by Eq. (8), written as,

$$\mathbf{R}_e^n(\tilde{\mathbf{q}}_p^n) = \frac{M}{\Delta t}\left(\frac{3}{2}\tilde{\mathbf{q}}_p^n\right) + \mathbf{R}(\tilde{\mathbf{q}}_p^n) - \frac{M}{\Delta t}\left(2\tilde{\mathbf{q}}_p^{n-1} - \frac{1}{2}\tilde{\mathbf{q}}_p^{n-2}\right) = 0 \tag{9}$$

where $\mathbf{R}_e^n$ represents the unsteady residual at time step n. To solve each implicit scheme efficiently, we employ a p-multigrid approach driven by a linearized Gauss-Seidel smoother [6].

Adjoint-Based Sensitivity Analysis

In the current work, surface nodes and additional surface quadrature points are deformed through the superposition of the Hicks-Henne bump function [10] placed at a set of designated surface nodes, and the deformations are related to the values of the corresponding design variables, $\mathbf{D}$. In response to changing locations of surface points, mesh points in the interior of the domain are deformed based on a linear tension spring analogy [11] to prevent the generation of overlapping elements. The resulting adjoint-based sensitivity derivative of a scalar-valued objective functional, L, with respect to the set of design variables is formulated by starting with the forward linearization and then performing a transpose operation to the problem. The discrete adjoint sensitivity formulation is shown in Eq. (10), while a detailed derivation can be found in Ref. [5].

$$\frac{dL}{d\mathbf{D}}^T = \left(\frac{\partial \mathbf{x}_s}{\partial \mathbf{D}}^T [K]^{-T} \frac{\partial \tilde{\mathbf{x}}}{\partial \mathbf{x}}^T + \frac{\partial \mathbf{x}_q}{\partial \mathbf{D}}^T \frac{\partial \tilde{\mathbf{x}}}{\partial \mathbf{x}_q}^T \right) \left(\frac{\partial L}{\partial \tilde{\mathbf{x}}}^T - \frac{\partial \bar{\mathbf{R}}_e}{\partial \tilde{\mathbf{x}}}^T \left[\frac{\partial \mathbf{R}_e}{\partial \tilde{\mathbf{q}}} \right]^{-T} \frac{\partial L}{\partial \tilde{\mathbf{q}}}^T \right) \tag{10}$$

It is noted that the objective sensitivities with respect to the mesh configuration must consider effects arising from both mesh grid points and additional surface quadrature points. $[K]$ refers to the stiffness matrix from the discrete mesh motion

equations, and $[\partial\bar{\mathbf{R}}_e/\partial\tilde{\mathbf{x}}]$ denotes the sensitivities of the unsteady residual with respect to the mesh configuration, whose contribution from time step n in the BDF2 scheme is obtained by,

$$\frac{\partial\bar{\mathbf{R}}_e^n}{\partial\tilde{\mathbf{x}}} = \frac{\partial\mathbf{R}_e^n}{\partial\tilde{\mathbf{x}}} + (\delta_{1n}+\delta_{2n})\left[\frac{\partial\mathbf{R}_e^n}{\partial\tilde{\mathbf{q}}^0}\right]\frac{\partial\tilde{\mathbf{q}}^0}{\partial\tilde{\mathbf{x}}} + \left[\frac{\partial\mathbf{R}_e^n}{\partial\mathbf{q}_b^n}\right]\frac{\partial\mathbf{q}_b^n}{\partial\tilde{\mathbf{x}}} \tag{11}$$

where δ represents the Kronecker-delta operator which takes on the value of 0 or 1, and the last two terms involve the explicit-dependence relations specified by the respective initial condition, $\tilde{\mathbf{q}}^0$, and unsteady boundary condition, $\mathbf{q}_b$. Returning to Eq. (10), to avoid a direct solve of the inverse of the transposed Jacobian matrix, the primal-adjoint variables are introduced, satisfying: $[\partial\mathbf{R}_e/\partial\tilde{\mathbf{q}}]^{-T}(\partial L/\partial\tilde{\mathbf{q}})^T = \lambda_{\mathbf{q}}$ or $[\partial\mathbf{R}_e/\partial\tilde{\mathbf{q}}]^T\lambda_{\mathbf{q}} = (\partial L/\partial\tilde{\mathbf{q}})^T$. A backward time-integration is used for solving the unsteady primal-adjoint solution, where the primal-adjoint solution at the final time step ($n=N$) is first solved, followed by the solutions at earlier time steps ($n = N-1, N-2, \cdots, 1$). In particular, the implicit BDF2 scheme for obtaining the the primal-adjoint solution is applied using the following sequential formulation:

$$\left[\frac{\partial\mathbf{R}_e^n}{\partial\tilde{\mathbf{q}}^n}\right]^T\lambda_{\mathbf{q}}^n = \frac{\partial L}{\partial\tilde{\mathbf{q}}^n}^T \qquad (n=N) \tag{12}$$

$$\left[\frac{\partial\mathbf{R}_e^n}{\partial\tilde{\mathbf{q}}^n}\right]^T\lambda_{\mathbf{q}}^n = \frac{\partial L}{\partial\tilde{\mathbf{q}}^n}^T - \left[\frac{\partial\mathbf{R}_e^n}{\partial\tilde{\mathbf{q}}^{n+1}}\right]^T\lambda_{\mathbf{q}}^{n+1} \qquad (n=N-1) \tag{13}$$

$$\left[\frac{\partial\mathbf{R}_e^n}{\partial\tilde{\mathbf{q}}^n}\right]^T\lambda_{\mathbf{q}}^n = \frac{\partial L}{\partial\tilde{\mathbf{q}}^n}^T - \left[\frac{\partial\mathbf{R}_e^n}{\partial\tilde{\mathbf{q}}^{n+1}}\right]^T\lambda_{\mathbf{q}}^{n+1} - \left[\frac{\partial\mathbf{R}_e^n}{\partial\tilde{\mathbf{q}}^{n+2}}\right]^T\lambda_{\mathbf{q}}^{n+2} \quad (1\le n\le N-2) \tag{14}$$

Thus the primal-adjoint solution at time step n ($n \le N-2$) requires the computed adjoint solution at its later time steps $n+1$ and $n+2$. A p-multigrid solver driven by a Gauss-Seidel smoother[6] is employed for solving the adjoint solution at each discrete time step location. Substituting the primal-adjoint variables into Eq. (10) yields,

$$\frac{dL}{d\mathbf{D}}^T = \frac{\partial\mathbf{x}_s}{\partial\mathbf{D}}^T[K]^{-T}\frac{\partial\tilde{\mathbf{x}}}{\partial\mathbf{x}}^T\frac{\partial\bar{L}}{\partial\tilde{\mathbf{x}}}^T + \frac{\partial\mathbf{x}_q}{\partial\mathbf{D}}^T\frac{\partial\tilde{\mathbf{x}}}{\partial\mathbf{x}_q}^T\frac{\partial\bar{L}}{\partial\tilde{\mathbf{x}}}^T \tag{15}$$

where

$$\frac{\partial\bar{L}}{\partial\tilde{\mathbf{x}}}^T = \frac{\partial L}{\partial\tilde{\mathbf{x}}}^T - \sum_{n=1}^{N}\frac{\partial\bar{\mathbf{R}}_e^n}{\partial\tilde{\mathbf{x}}}^T\lambda_{\mathbf{q}}^n \tag{16}$$

Furthermore, by introducing a mesh-adjoint variable satisfying $[K]^T\lambda_x = (\frac{\partial\tilde{\mathbf{x}}}{\partial\mathbf{x}})^T(\frac{\partial\bar{L}}{\partial\tilde{\mathbf{x}}})^T$, the final formulation for evaluating sensitivity derivative via the discrete adjoint approach is expressed as:

$$\frac{dL}{d\mathbf{D}}^T = \frac{\partial\mathbf{x}_s}{\partial\mathbf{D}}^T\lambda_x + \frac{\partial\mathbf{x}_q}{\partial\mathbf{D}}^T\frac{\partial\tilde{\mathbf{x}}}{\partial\mathbf{x}_q}^T\frac{\partial\bar{L}}{\partial\tilde{\mathbf{x}}}^T \tag{17}$$

The current work employs the PORT trust region optimization strategy[12] to obtain a new set of design variables. A typical design iteration follows the procedure shown in Fig. 1. The main cost of one design iteration arises from both the electromagnetic solution and the primal-adjoint solutions, which are roughly equivalent for the unsteady case considered in the present work.

Numerical Examples

A spatial accuracy examination for the discontinuous Galerkin Maxwell solver is first conducted using a rectangular waveguide along with the assumption that the electric field is transverse to the direction of propagation. An exact solution of this problem is readily available and is given by[13]:

$$D_x(\mathbf{x},t) = -\frac{B_0\beta}{\omega\mu}\cos(\alpha x)\sin(\beta y)\sin(\omega t) \tag{18}$$

$$D_y(\mathbf{x},t) = \frac{B_0\alpha}{\omega\mu}\sin(\alpha x)\cos(\beta y)\sin(\omega t) \tag{19}$$

$$B_z(\mathbf{x},t) = B_0\cos(\alpha x)\cos(\beta y)\cos(\omega t) \tag{20}$$

where $\alpha = m\pi/x_L$, $\beta = n\pi/y_L$ and $\omega = \sqrt{(\alpha^2+\beta^2)/\varepsilon/\mu}$. B_0 refers to the amplitude of the magnetic flux density, which is set to be 1 in this case. $m/2$ and $n/2$ denote the number of waves in the x and y directions of the computation domain $\{(x,y)|\ 0<x<x_L, 0<y<y_L\}$. In the following we set m and n to be 16 and 10, respectively. A perfect conducting

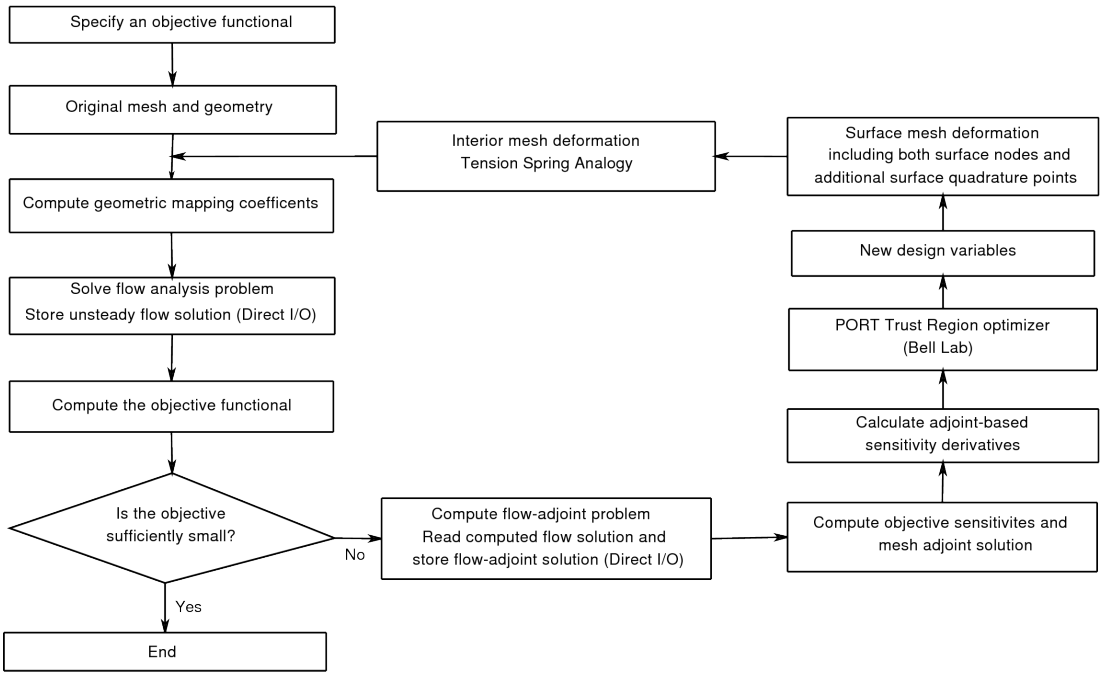

Figure 1. Illustration of the optimization algorithm.

wall condition is applied to all computational domain boundaries and the Roe Riemann flux approximation[9] is employed at the interior elemental boundaries. Contours of the magnetic flux density after one period ($t = T$) are illustrated in Fig. 2, using a p= 4 spatial DG discretization (fifth-order accurate) and the BDF2 implicit temporal scheme with a time-step size of $\Delta t = 0.01$. Note that each wave in the y direction, for example, is resolved by only about three elements. Fig. 3(a) displays a more quantitative comparison, where profiles of the magnetic flux density along $x = 40$ are compared with the exact solution at $t = T$ as well as $t = 10T$. It can be observed that the fifth-order DG solution exhibits very good accuracy, where there is no visual deviation between the computed and exact solutions, even for the longer time-integration case. Three grids, consisting of 1600, 2500 and 6400 structured triangular elements, are used to examine convergence of the spatial discretization error of the DG schemes ranging from p= 1 to p= 4. Here, the BDF2 temporal scheme is used to obtain the unsteady electromagnetic solution, with a time-step size sufficiently small to ensure that the temporal error has a negligible contribution to the total error. Fig. 3(b) shows the convergence of the spatial discretization error as a function of grid spacing for various orders of DG discretization in the TE wave test case. The L_2 norm of the solution error is measured at about $t = T/2$ with the corresponding exact solution, in which the optimal error convergence rate ($\sim h^{p+1}$) is approximately attained in this study. In particular, the asymptotic slopes of the p=1, p=2, p=3 and p=4 DG schemes are 2.209, 3.165, 4.030 and 4.970, respectively, which are close to the respective design values of 2 3, 4, and 5.

The next example considers an unsteady shape optimization case for an electromagnetic scattering problem, in which the adjoint-based sensitivity technique discussed previously is used to calculate the objective gradients at each design iteration. The goal of this shape optimization case is to match a time-dependent magnetic-field profile on the target NACA65(1)-212 airfoil by changing the shape of the original NACA0012 airfoil geometry. The objective functional for this purpose is defined as,

$$L = \sqrt{\frac{\sum_{n=1}^{N}\sum_{i=1}^{N_s}(B_{z_i}^{n} - B_{z_i}^{*n})^2}{N \times Ns}} \tag{21}$$

where $B_{z_i}^{n}$ and $B_{z_i}^{*n}$ denote the values of the magnetic solution at time step n for surface point i on the respective current and target airfoil surfaces. N and N_s represent the total number of time steps and the number of surface grid points. A computational mesh containing 4367 unstructured triangular elements is employed, along with 118 design variables spanning about 99% of the chord locations on the upper and lower airfoil surfaces. The surface deformation occurs in the y-coordinate direction alone since it is not desired to change the chord length of the airfoil. A fifth-order DG scheme (i.e. p = 4) and the BDF2 temporal scheme with a time-step size of $\Delta t = 8 \times 10^{-3}$ are used for the respective spatial and temporal discretizations. An initial electromagnetic-field solution (i.e. $t = 0$) is prescribed ahead of the airfoil and is allowed to propagate downstream, thereby impacting the airfoil. This initial distribution is given by,

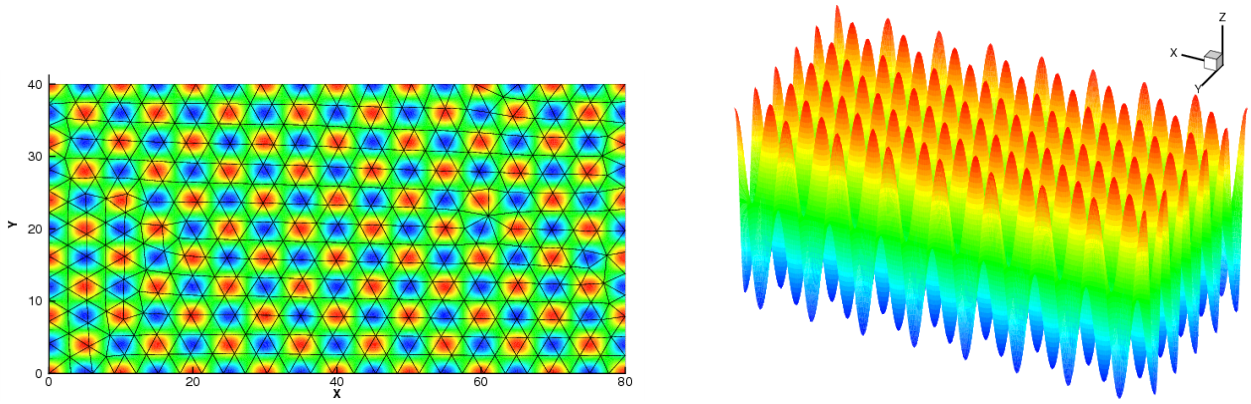

(a) Computational mesh and magnetic field solution

(b) 3D-view of the magnetic field solution

Figure 2. Computational mesh (containing 803 elements) and magnetic field solution for a transverse electric wave at $t = T$ using a $\mathrm{p} = 4$ (i.e. fifth-order accurate) spatial DG discretization and the BDF2 implicit scheme, where approximately three elements are employed to resolve each wave in the y direction.

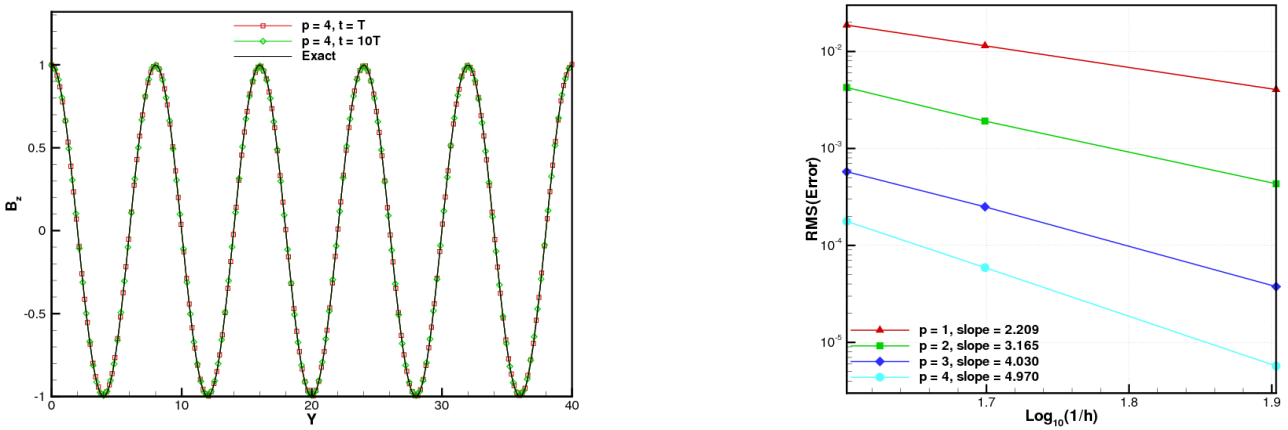

(a) Magnetic solution profiles

(b) Spatial discretization error vs. grid spacing

Figure 3. (a) Comparison of magnetic-field solution at $t = T$ and $t = 10T$ with the exact solution, using a $\mathrm{p} = 4$ spatial DG discretization and the BDF2 implicit scheme. (b) Convergence of spatial discretization error for various orders of DG discretization as a function of grid spacing in the TE wave example.

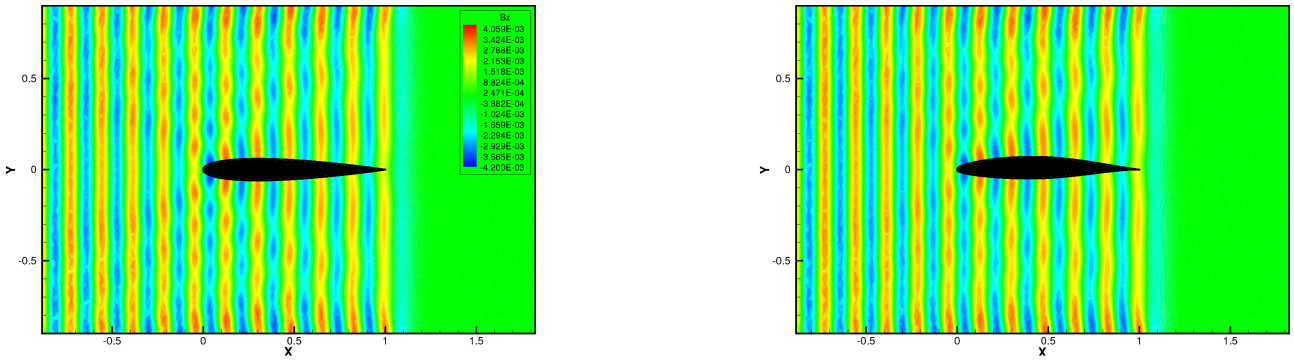

(a) Original NACA0012 airoil

(b) Target NACA65(1)-212 airfoil

Figure 4. Contours of the magnetic flux density for the original NACA0012 airfoil (a) and the target NACA65(1)-212 airfoil (b) at final time $t = 1.2$ in the electromagnetic scattering problem, using a $\mathrm{p} = 4$ spatial DG discretization and the BDF2 scheme.

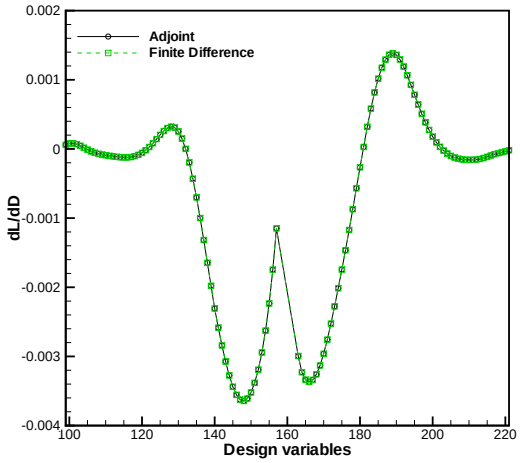

Figure 5. Comparison of sensitivity derivative vector using the unsteady discrete adjoint method and the finite-difference method for the original mesh and airfoil geometry.

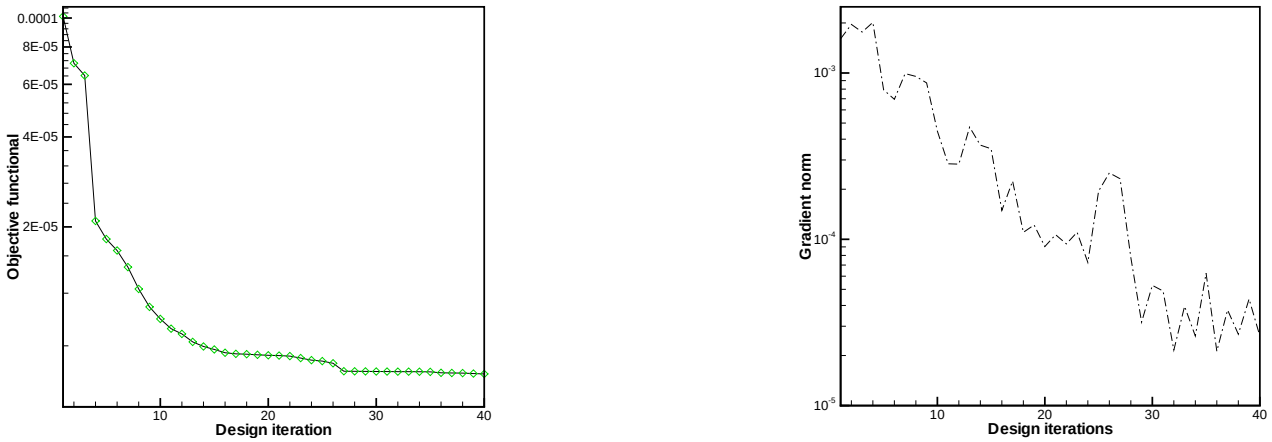

(a) Convergence of objective functional

(b) Convergence of gradient norm

Figure 6. Convergence of the objective functional and gradient norm in terms of the number of design iterations in the electromagnetic shape optimization case.

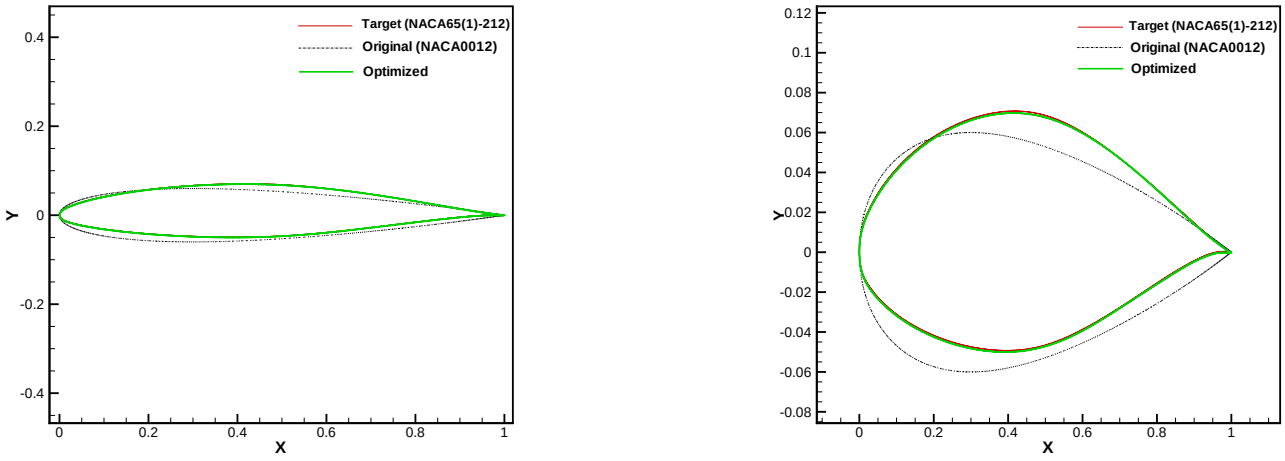

(a) 1:1 scale

(b) Exaggerated scale

Figure 7. Comparison of airfoil shapes among the target NACA65(1)-212 airfoil, the original NACA0012 airfoil and the final optimized airfoil in the electromagnetic shape optimization case.

$$\left.\begin{array}{l} D_x(\mathbf{x}) = 0 \\ D_y(\mathbf{x}) = D_0 \cos(\alpha(t-x)) \\ B_z(\mathbf{x}) = B_0 \cos(\alpha(t-x)) \end{array}\right\} \text{ for } x < x_w = -\frac{\pi}{2\alpha}, \text{ otherwise } D_x(\mathbf{x}) = D_y(\mathbf{x}) = B_z(\mathbf{x}) = 0 \tag{22}$$

where D_0 and B_0 denote the amplitudes of the respective electric and magnetic waves, and α relates to the frequency of the wave, which is set to be 36 in the scattering problem. x_w indicates the x-coordinate location where the electromagnetic waves start to propagate. The airfoil surface is treated as a perfect electric conductor and the Dirichlet boundary condition, as specified by Eq. (22), is imposed on the outer boundaries, while interior fluxes are computed based on the Lax-Friedrichs Riemann flux approximation[8]. Fig. 4 illustrates contours of the magnet flux density at the final time $t = 1.2$ (i.e. $N = 150$) for the original NACA0012 airfoil and the target NACA65(1)-212 airfoil in the test case specified. Validation of the sensitivity calculation using the developed adjoint method is illustrated in Fig. 5 by comparing to finite-difference gradients. One can observe that the adjoint-based sensitivity derivative provides an excellent match with the finite-difference results, thus verifying the sensitivity formulation derived in this work. Fig. 6 plots the convergence of the objective functional and gradient norm against the number of shape optimization iterations, where it is shown that over a one-order magnitude reduction in the objective and an approximately two-order magnitude reduction in gradient norm are obtained in 40 design steps. Fig. 7 compares the geometry shapes for the original, target and final optimized airfoils using a 1:1 scale as well as an exaggerated vertical scale to show more details. One can observe that the consequent optimized airfoil shape matches with the target geometry very well, although the original symmetric shape differs considerably with the target.

Conclusions

This report presents a discrete adjoint algorithm for calculating sensitivity information in electromagnetic shape optimization problems. A high-order accurate discontinuous Galerkin method is used for solving the model electromagnetic problems, with incorporation of a second-order backward Euler scheme to obtain the unsteady electric- and magnetic-field solution in the time domain. Convergence of the spatial discretization error has been examined in the current work where the optimal error convergence ($\sim h^{p+1}$) is achieved. Due to the fact that curvilinear boundary elements are employed near complicated geometries, special treatments are required for variation and re-creation of curved boundary elements to maintain the design order of accuracy for the scheme. These treatments must also be reflected in the linearization of the objective functional to obtain consistency with the analysis code. Results on an electromagnetic scattering shape optimization case further provide verification of the discrete adjoint sensitivity formulation developed in this work. The adjoint-based optimization algorithm performs efficiently for a large number of input variables, thus becoming an important approach for electromagnetic design problems. Future work will concentrate on the development of shape and material design techniques in three-dimensional electromagnetic problems.

Acknowledgments

The work was supported by the Tennessee Higher Education Commission (THEC) Center of Excellence in Applied Computational Science and Engineering (CEACSE). The support is greatly appreciated.

References

[1]B. Cockburn, C.-W. Shu, The local discontinuous Galerkin method for time-dependent convection-diffusion systems, SIAM J. Numer. Appl. Mech. Engrg. 35 (1998) 2440–2463.

[2]F. Bassi, A. Crivellini, D. A. D. Pietro, S. Rebay, An implicit high-order discontinuous Galerkin method for steady and unsteady incompressible flows, Comput. Fluids 36 (10) (2007) 1529–1546.

[3]P.-O. Persson, J. Bonet, J. Peraire, Discontinuous Galerkin solution of the Navier-Stokes equations on deformable domains, Comp. Methods Appl. Mech. and Engrg. 198 (17-20) (2009) 1585–1595.

[4]J. S. Hesthaven, T. Warburton, Nodal high-order methods on unstructured grids. i. time-domain solution of maxwell's equations, J. Comput. Phys. 181 (1) (2002) 186–221.

[5]L. Wang, Techniques for high-order adaptive discontinuous Galerkin discretizations in fluid dynamics, Doctoral Dissertation, Department of Mechanical Engineering, University of Wyoming (May 2009).

[6]L. Wang, D. J. Mavriplis, Implicit solution of the unsteady Euler equations for high-order accurate discontinuous Galerkin discretizations, J. Comput. Phys. 225 (2) (2007) 1994–2015.

[7]C. R. Nastase, D. J. Mavriplis, High-order discontinuous Galerkin methods using an *hp*-multigrid approach, J. Comput. Phys. 213 (1) (2006) 330–357.

[8]C.-W. Shu, Essentially Non-oscillatory and Weighted Essentially Non-oscillatory Schemes for Hyperbolic Conservation Laws, ICASE Report No. 97-65, NASA/CR-97-206253, 1997.

[9]P. L. Roe, Approximate Riemann solvers, parameter vectors, and difference schemes, J. Comput. Phys. 43 (2) (1981) 357–372.

[10]R. M. Hicks, P. A. Henne, Wing design by numerical optimization, J. Aircraft 15 (7) (1978) 407–412.

[11]Z. Yang, D. J. Mavriplis, Unstructured dynamic meshes with higher-order time integration schemes for the unsteady Navier-Stokes equations, AIAA Paper 2005-1222 (Jan 2005).

[12]P. A. Fox, A. D. Hall, N. L. Schryer, The PORT mathematical subroutine library, ACM TOMS 4 (1978) 104–126.

[13]M. F. Iskander, Electromagnetic Fields and Waves, Waveland Press, Inc., 1992.